RESEARCH ARTICLE

Key Points:
- Hiss generated huge precipitations in afternoon sector at high latitude
- Localized concurrent Pc5 oscillations in geomagnetic field and CNA during recovery phase of 17 March 2015 storm
- Use of transfer entropy method

Supporting Information:
- Movie S1
- Movie S2

Correspondence to:
J. K. Behera,
jayanta.sssj@gmail.com

Enhancement and modulation of cosmic noise absorption in the afternoon sector at subauroral location ($L = 5$) during the recovery phase of 17 March 2015 geomagnetic storm

Jayanta K. Behera[1,2], Ashwini K. Sinha[1], Geeta Vichare[1], Ankush Bhaskar[1] [ID], Farideh Honary[3] [ID], Rahul Rawat[1], and Rajesh Singh[4] [ID]

[1]Indian Institute of Geomagnetism, New Bombay, India, [2]Pillai HOC College of Arts, Science and Commerce, Rasayani, India, [3]Department of Physics, Lancaster University, Lancaster, UK, [4]Dr. K.S. Krishnan Geomagnetic Research Laboratory (KSKGRL), Allahabad, India

Abstract The present study has focused on the intense production of cosmic noise absorption (CNA) at Maitri, Antarctica ($L = 5$; CGM −62°S, 55°E) during the early recovery phase of the largest storm of the current solar cycle commenced on 17 March 2015 St. Patrick's Day. The enhancement of CNA during 15–18 UT(14–17 magnetic local time (MLT); MLT = UT − 1 at Maitri) was as large as the CNA enhancement occurred during the main phase of the storm. During this time the CNA pattern also exhibits oscillation in the Pc5 (2–7 mHz) range and is in simultaneity with geomagnetic pulsations in the same frequency range. We observed the amplitude of CNA pulsation is well correlated with the level of CNA production. High-amplitude Pc5 oscillations were observed in the vicinity of auroral oval near Maitri. Absence of electromagnetic ion cyclotron (EMIC) waves is marked suggesting the possible role of VLF waves in precipitation. The reason for the intense CNA production is found to be the precipitation caused mainly by hiss-driven subrelativistic electrons. The CNA enhancement event is located well inside the dusk plasmaspheric bulge region as suggested by Tsurutani et al. (2015). Signature of enhanced eastward electrojet at Maitri during 14–17 MLT could be an additional factor for such large CNA. In order to establish the cause and effect relationship between the geomagnetic and CNA oscillations at Maitri, transfer entropy method has been used, which confirmed the modulation of CNA by geomagnetic pulsations.

1. Introduction

The precipitation of energetic particles at the high-latitude atmosphere, associated dynamics, and chemical changes are important aspects of space weather research. Charged particle precipitation is associated with the coupling process between Van Allen radiation belts and the Earth's high-latitude atmosphere. Study of precipitation process has been recently getting attention from the space and climate research point of view. Not only will the study provide physics of the radiation belts and related energetic electron flux evolution but will throw light on the link between the atmospheric precipitation of solar energetic particles and polar climate variability [e.g., *Tsurutani et al.*, 2016; *Rodger et al.*, 2013; *Seppälä et al.*, 2007; *Turunen et al.*, 2009]. It has been seen that energetic electron precipitation enhances the photochemistry that produces odd nitrogen and odd hydrogen in the atmosphere. They couple with the polar vortex and catalytically destroy ozone [e.g., *Tsurutani et al.*, 2016; *Rodger et al.*, 2013, and references therein].

Predominantly, ULF magnetic pulsations play a major role in the acceleration and loss of high energetic electrons in the dawn sector of auroral oval. These ULF waves, together with VLF chorus waves, result in high-latitude precipitations. In fact, both chorus and hiss can drive particle precipitation at higher L values [e.g., *Li et al.*, 2015; *Gołkowski and Inan*, 2008; *Bortnik and Thorne*, 2007]. The main mechanism behind such precipitation is the electron-cyclotron resonance and subsequent pitch angle diffusion [*Kennel and Petschek*, 1966; *Tsurutani and Lakhina*, 1997]. The theoretical explanation as well as modeling of cyclotron resonance of precipitating energetic electrons from tens of keV to more than 1 MeV with VLF waves has been reported by *Bortnik and Thorne* [2007]. However, *Tsurutani et al.* [2013] argued that chorus may not be responsible for relativistic electron precipitation. Recently, *Remya et al.* [2015] has clearly shown that the role of EMIC waves

is more significant as compared to chorus in the precipitation of relativistic electrons. *Tsurutani et al.* [1979] have shown for the first time that anisotropic electrons can generate chorus waves, thus informing the loss cone instability for the production of chorus waves. Further, *Tsurutani and Smith* [1977] have analyzed the latitudinal and local time distribution of these extremely low frequency (10–1500 Hz) chorus to determine their dependence on substorms and showed that equatorial chorus is associated with substorm activities. In this study VLF-hiss was observed during the substorm activity at high latitude. Other study shows that interaction of relativistic electrons and protons with electromagnetic ion cyclotron (EMIC) waves in the inner magnetosphere also give rise to significant precipitation [*Rodger et al.*, 2008; *Miyoshi et al.*, 2008]. Generally, EMIC waves fall at highest frequency band in the ULF spectral regime. They are observed as Pc1 and Pc2 geomagnetic oscillations at the ground. *Anderson et al.* [1992] have examined AMPTE satellite mission data, which showed that EMIC wave predominantly occurs on the dayside and afternoon/dusk sector. However, later it was confirmed with a statistical study done by *Meredith et al.* [2003] that occurrences of EMIC waves are restricted to dusk sector. EMIC waves are mostly responsible for scattering of protons during storm and substorm processes and are considered as potential cause of ring current ion loss during strong geomagnetic activities. Protons within energy band of 10–100 keV undergo proton cyclotron instability with EMIC wave causing the pitch angle diffusion and subsequent loss [*Yahnina et al.*, 2003; *Yahnin and Yahnina*, 2007; *Yahnin et al.*, 2007]. *Criswell* [1969] and *Kawamura et al.* [1982] have shown the approximate occurring location of EMIC waves to be at $L \sim 2–5$.

Occurrence of geomagnetic pulsations in the Pc5 (2–7 mHz) range during the recovery phase of a geomagnetic storm is well established. Many workers [*Yumoto and Saito*, 1980; *Kivelson and Zu-Yin*, 1984] have suggested that the solar wind-driven Kelvin-Helmholtz instability (KHI) at the magnetopause leads to such pulsations at the magnetopause. *Pilipenko et al.* [2010] have shown that the generation of Pc5 waves can be caused by high speed solar wind stream and elevated density fluctuation triggered by KHI. Additionally, *Pilipenko* [1990] has shown that Pc5 waves can be effectively triggered by energetic proton fluxes with non-Maxwellian distribution in energy and space. However, a statistical study by *Viall et al.* [2009] showed certain discrete frequencies in the solar wind are more favorable to produce Pc5 pulsations in the magnetosphere, globally. Moreover, *Behera et al.* [2016] have shown that presence of Pc5 pulsation at high latitude coincides with particle precipitation phenomena.

Normally, substorm onset, geomagnetic pulsations, whistler mode VLF chorus, and energetic particle precipitation are simultaneous phenomena observed in the morning sector at auroral latitudes. Sometimes, pulsations are also seen in the cosmic noise absorption (CNA) event. *Senior and Honary* [2003] have shown that electron precipitation as seen in CNA data has been modulated by geomagnetic pulsations. In that study, IRIS for CNA observation and IMAGE chain magnetometers for geomagnetic pulsation observation have been used, respectively. A statistical study was done by *Spanswick et al.* [2003] using NORSTAR riometer and CANOPUS magnetometer arrays in order to understand the modulation of high-energy electron precipitation by ULF waves in the Pc5 frequency band. The study was conducted in two parts. One part has explained the necessary conditions, i.e., presence of geomagnetic pulsation for the occurrences of pulsation in CNA . The study has used 11 years of CNA and geomagnetic data from three different stations. They also observed that 95% of CNA pulsations occur during morning hour compared to 70 % geomagnetic pulsations. The study revealed that for a geomagnetic pulsation that occurs in an auroral location during dawn hours, 70% chances are there to occur a corresponding CNA pulsation. Therefore, it is concluded that CNA pulsation needs both favorable magnetospheric electron flux conditions and large enough magnetic Pc5 wave activity. Following the data survey of *Baker et al.* [2003], it was suggested that pulsations generated due to field line resonances are more likely to cause CNA pulsations as observed by Riometer.

CNA is mostly related to *D* region ionization due to particle precipitation at high latitude [*Little and Leinbach*, 1958; *Ansari*, 1964]. However, there are various processes that may give rise to CNA events. A complete description of such processes were provided by *Stauning* [1996]. With the help of simple wide beam riometer data in earlier days, it was easy to calculate the CNA value just by subtracting the quiet day radio signal from the radio signal of any arbitrary disturbed day [*Little and Leinbach*, 1959]. But it was not sufficient in order to retrieve any spatial or temporal information of CNA pattern. *Detrick and Rosenberg* [1990] proposed an advanced Riometer (called *imaging riometer*) which can provide two-dimensional image of CNA within the field of view (FOV). They constructed multiple narrow beam arrays with the individual antenna elements. It was done by the combination of receiving signals with proper phase shifting so that beams can be pointed to different directions. A more advanced beam forming done digitally has led to digital imaging riometers such as Maitri [see *Honary et al.*, 2011].

So far, many workers have shown the different aspects of the St. Patrick's Day geomagnetic storm of March 2015. *Sripathi et al.* [2015] has shown low-latitude impact within the Indian sector. *Tulasi Ram et al.* [2016] has shown the pronounce equatorial zonal electric field enhancement in response to prompt penetration of eastward convection electric fields (PPEFs) during this geomagnetic storm which is in agreement with the case study of a interplanetary shock event of 5–6 November 2001 that caused ionospheric upliftment at dayside equatorial and midlatitude ionosphere [*Tsurutani et al.*, 2004]. Similar study was also done by *Iijima et al.* [2005]. *Cherniak and Zakharenkova* [2015] and *Astafyeva et al.* [2015] have shown the high-latitude impact during the main phase of the storm. This work is mainly based on the observations during the early recovery day (18 March 2015) of the St. Patrick's geomagnetic storm. The main phase has been explained in great detail by above workers. Detail elaboration of the 2015 storm has been mentioned by *Kamide and Kusano* [2015]. Significant information regarding solar wind-driven ionosphere-thermosphere coupling can be obtained during three storms near 2012, 2013, and 2015 St. Patrick's Day [*Verkhoglyadova et al.*, 2016]. This largest storm of the current solar cycle also has an extended recovery phase up to 10 days.

In this study, we have concentrated on the early recovery phase of the storm. Sudden enhancement in CNA was observed at postnoon hours (1500–1800 UT) of 18 March 2015 at Maitri, Antarctica, with signature of eastward electrojet along with VLF-hiss signature at Halley station (geographic 75.58°S, 26.233°W). Understanding the cause of such huge CNA enhancement during afternoon hours at $L = 5$ and the underlying processes that caused such particle precipitation form the main theme of the work. Further, we also observe the presence of geomagnetic as well as CNA pulsations during that period. Characteristic study of these pulsations during this period has been examined in corroboration with IMAGE chain stations. We have also tried to identify the cause and effect relationship between the geomagnetic pulsation and CNA pulsation at Maitri. For this purpose, we have used a novel technique based on transfer entropy method.

2. Data Set

A 4×4 imaging riometer operating at 38.2 MHz was installed at Indian Antarctic station Maitri ($L = 5$; CGM 62°S, 55°E) in February 2010. It passively receives stellar cosmic noise signal with 1 Hz sampling rate. It is used for the study of characteristics and dynamics of cosmic noise absorption (CNA) events and related space weather activities. Use of imaging riometer has significant advantages over a simple riometer. Imaging can be done with the help of 16 narrow beams, and wide beam can also be constructed. Details of the beam forming for the imaging riometer has been well explained by *Honary et al.* [2011]. The field of view (FOV) of the imaging riometer is 200 km × 200 km at 90 km altitude. For more than a decade, the variation in all three geomagnetic components has been recorded by Digital Fluxgate Magnetometer (DFM) installed at the same location (Maitri) of Imaging Riometer in Antarctica by Indian Institute of Geomagnetism. The collected data of DFM is of 1 Hz resolution. Here imaging riometer data and DFM data have been used to study the CNA event and auroral electrojet characteristics, respectively, during the period of our interest.

The interplanetary parameters during the St Patrick's Day storm have been collected from the OMNIWEB site (http://omniweb.gsfc.nasa.gov/ow_min.html) for a period of 3 days (17–19 March 2016). The website provides the time-shifted interplanetary data to the Earth's bow shock nose with high resolution (1 min and 5 min) as well as low resolution (hourly). The collected parameters are solar wind velocity (V_s), interplanetary magnetic field (B_z and B), solar wind density(n_s), pressure(P_S), etc. Geomagnetic storm and substorm signatures are studied with the help of ground geomagnetic indices such as AL, *SYM-H*, and *Dst*, which are collected from the WDC, Kyoto, website (http://wdc.kugi.kyoto-u.ac.jp/wdc/Sec3.html).

Identification of substorm event and its onset is still a debatable issue. Wave and planetary (W_p) index introduced by *Nosé et al.* [2012] indicates substorm onsets more accurately [*Thomas et al.*, 2015]. This index is based on the wave power of the Pi2 waves by taking geomagnetic data from the 11 stations of low to middle latitude. Local variation in the H component data is obtained from DFM, and wide beam and image of CNA are taken from imaging riometer operating simultaneously at Maitri.

The magnetic field variations and energetic electron flux can be obtained from the magnetometer (MAG) and Energetic Particle Sensor (EPS) on board Geostationary Operational Environmental Satellite (GOES). This study has used energetic electron flux data of energetic particle sensor (EPS) from GOES 13 and GOES 15 satellites. These GOES satellites are geosynchronous at an altitude of ∼36,000 km with 75° west and 135° west longitude, respectively. Energetic proton, electron, and alpha detector (EPEAD) on board GOES detects integral electron flux ($E > 0.8$ MeV, $E > 2.0$ MeV) and EPS detects electron flux of energy band of 40–475 keV. These data could

be obtained from CDAWEB website of NASA (http://cdaweb.gsfc.nasa.gov). In this study, we have used 1 min electron flux data of $40-475$ keV energy band from GOES 13 and GOES 15 EPS detector.

In order to study the presence of auroral electrojets within the auroral oval, we have used IMAGE chain magnetometer data. Characteristics of geomagnetic pulsations in Pc5 range ($2-7$ mHz) have also been analyzed with the help of IMAGE chain magnetometer. We envisage that event which has been studied in this paper is directly related to wave-particle processes within the inner magnetosphere. Hence, VLF observation was required for this study. Unfortunately, VLF data were not available during this event at Maitri, Antarctica. In order to compensate and complement our observations, summary plots of VLF observation from the Halley station (geog. 75.58°S, 26.233°W) are used in this study.

The presumption of such huge CNA that was recorded by imaging riometer due to wave-particle interaction has motivated us to look for multisatellite observations of wave activities during the event period. Therefore, we examined the numbers of available satellites orbiting during the period of our interest ($15-18$ UT on 18 March 2015). We used 4-D Orbit Viewer (an interactive visualization of satellite orbits) software provide by NASA (https://sscweb.gsfc.nasa.gov/tipsod/) to locate all the satellites during the event periods. We found that Van Allen Probes, or popularly known as Radiation Belt Storm Probes satellites (RBSP), and a couple of Time History of Events and Macroscale Interactions during Substorms (THEMIS) satellites were orbiting in favorable L values. Since, RBSP-A was approaching dawn during the event hours where the event apparently took place in the dusk hours, we neglected the observations of RBSP-A. However, the power spectral distribution (PSD) of electric field and PSD of magnetic field data of RBSP-B data were used to identify the wave activities. Additionally, the average electron and ion energy eflux spectrograms derived from SST full distribution data from THEMIS-A (P5) and THEMIS-D (P3) were analyzed. The plots were generated from CDAWEB website of NASA (http://cdaweb.gsfc.nasa.gov).

3. Observations

Figure 1 provides the interplanetary conditions and the ground observations during the 2015 St. Patrick's Day geomagnetic storm which was the largest geomagnetic storm ($Dst < -221$ nT) of the current solar cycle.

3.1. The 17 March 2015 Geomagnetic Storm Event

Our interest lies in the first day of the recovery phase, and hence, importance is also given to the interplanetary and ground observation of the first day of the recovery phase (18 March 2015) in details.

The storm which started on 17 March 2015 on St. Patrick's Day is classified as G4 (severe) level storm (http://www.swpc.noaa.gov/noaa-scales-explanation). Interestingly, the $17-18$ March 2015 storm was not associated with any major X-class or M-class flare *Kamide and Kusano* [2015] which is generally prescribed as precursor. Figure 1 illustrates the St. Patrick's storm during $17-19$ March 2015. Figure 1 (first to fourth rows) represents the interplanetary conditions such as solar wind velocity (V_s), interplanetary magnetic field B and its southward component IMF B_z, plasma density (n_s), and solar wind pressure (P_s). Figure 1 (fifth and sixth rows) shows the ground signatures. AL and AE show the localized disturbances in the auroral oval. Global response of this geomagnetic storm can be seen in Dst index. This storm was marked by (SI$^+$) causing a shock at $\sim$0445 UT followed by the main phase has started which can be seen in Dst index in the last two panels, respectively. The main phase Dst has dropped down to its minimum value of -226 nT at $\sim$2300 UT with couple of localized depressions of -93 nT and -164 nT at $\sim$0940 UT and $\sim$1740 UT, respectively [*Verkhoglyadova et al.*, 2016; *Cherniak and Zakharenkova*, 2015]. Interplanetary behavior was very dynamic in the main phase of the storm. Solar wind velocity started increasing at $\sim$0445 UT up to 1600 UT and showed slow decline up to 2400 UT of 17 March 2015. Later on, it started slowly increasing and maximize at $\sim$2100 UT of 28 March 2015. Interplanetary magnetic field showed enhancement right after the SI^+ and maximized up to 20 nT at 1500 UT. In particular, IMF B_z was very much fluctuating during the main phase. The details of these fluctuations were provided by *Verkhoglyadova et al.* [2016] and *Astafyeva et al.* [2015]. During the recovery phase, IMF B_z was still fluctuating but with less intensity. The minimum value of IMF B_z was ~ -10 nT which was almost half of the intensity of IMF B_z observed during the main phase. Solar wind density and solar wind pressure showed steady behavior right after the end of main phase. The average values of solar wind density and solar wind pressure during the first day of the recovery phase were less than half of those observed during the main phase. The ground observations were also in agreement with the above observations. Auroral indices AL/AE showed significant reduction/enhancement during the main phase in comparison to the recovery phase. For the present storm, minimum value of AL was ~ -2000 nT and maximum value of AE was $\sim$2000 nT
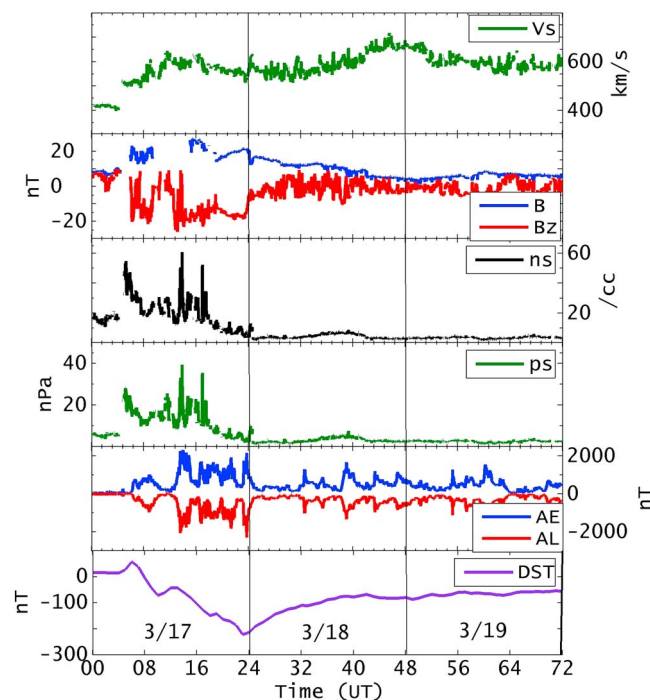
Figure 1. Variation in the interplanetary and ground observations during 17–19 March 2015 St. Patrick's geomagnetic storm. (first to fourth rows) The 1 min resolution interplanetary parameters data such as solar wind velocity (V_s), IMF (B), the southward component of IMF (B_z), solar wind density (n_s), and solar wind pressure (P_s). (fifth row) The variation in AE and AL indices. (sixth row) The Dst index.

during the main phase, whereas AL was ~ −1200 and AE was ~1200 nT during the first recovery phase (18 March 2015). Nevertheless, out of many substorms during first recovery phase, the largest substorm occurred during ~1400–1800 UT. During the onset of the substorm, W_p index was significant (~0.7 nT). In order to explain the energy that enters into the magnetosphere during solar wind-magnetosphere coupling, *Astafyeva et al.* [2015] have explained the behavior of polar cap index (*PC*). Furthermore, close observation of *PC* index clearly showed less enhancement during the first recovery phase of the storm. These acts suggest that the energy transfer into the magnetosphere during the first recovery day onward has reduced significantly. However, the observation at Maitri during the first day of the recovery phase revealed a huge CNA event, which was even more than the CNA occurred at Main phase of the storm. The paper considers this anomalous behavior of the CNA intensity.

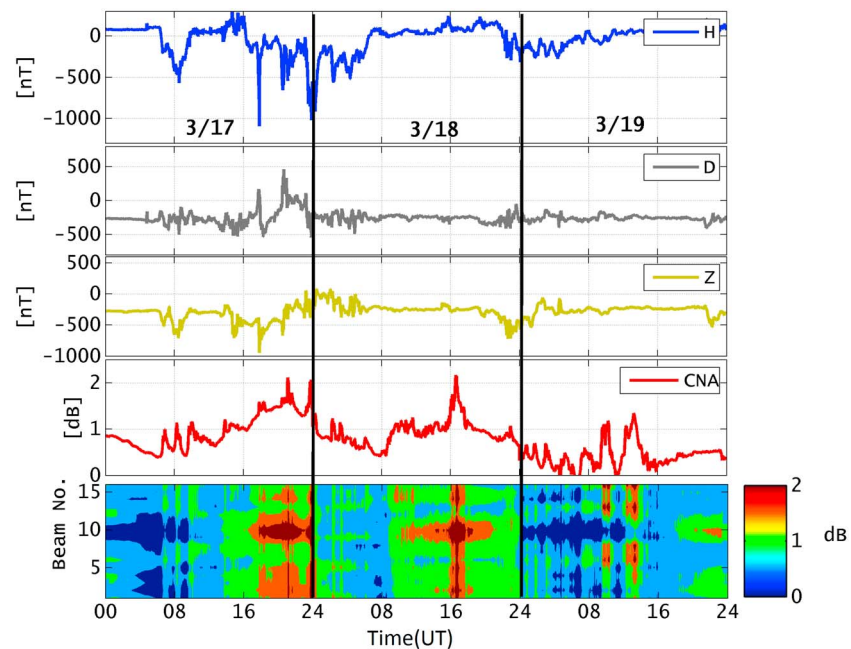This geomagnetic storm was associated with a number of substorm onsets which is not unusual for severe geomagnetic storm. In order to find the substorm onset, one can follow the articles such as [*Singh et al.*, 2012; *Behera et al.*, 2015], where the detailed criteria for identification of substorms has been explained. Figure 1 shows the number of substorm onsets during the storm. It is clearly observed that the intensity and number of substorms gets reduced with the proceeding of the storm. The main phase of storm is associated with intense substorms as shown in Figure 1 (fifth row). The main phase sustained up to almost midnight (2400 UT) of 17 March end then recovery has started. The concurrent auroral electrojet signatures were stronger and more frequent, whereas there were hardly any auroral electrojet intensification up to 0600 UT of 18 March. The auroral electrojets started appearing only after ~0600 UT but with relatively low strength. This continues till the recovery of the storm.

3.2. Observation at Maitri During the Storm

Figure 2 depicts the multi-instrumental observations at Indian Antarctic station, Maitri, during the period of 17–19 March 2015. The CNA data were obtained by subtracting the riometer signal for the disturbed days (17–19 March) from the QDC of the March month of 2015. Figure 2 (fifth row) is showing the keogram of the imaging riometer which provides the image plot CNA across a field of view of ~200 × 200 km over Maitri at 90 km height. The keogram is produced by the contour map of all the beam with zero zenith corrections. Significant intensification of westward electrojet is evident from the depression in the *H* component during the main phase with multiple substorm activities as shown in Figure 2 (first row). Often the intensification of westward electrojet correlates well with the substorm onset during midnight to morning hours [*Behera et al.*, 2015]. The first onset of westward electrojet that is seen ~0700 UT just coincides with the substorm onset during the main phase of the storm. The next large westward electrojet intensification is seen ~1600 UT of 17 March to 0800 UT of 18 March centered at midnight. Similarly, westward electrojet intensification is seen during 2000 UT of 18 March to 0800 UT of 19 March. Note that intensification of westward electrojet has drastically reduced. The maximum electrojet value was −1200 nT centered at 17 March midnight, whereas it was only −300 nT for the next midnight. At Maitri, CNA enhancement is seen right from the first onset of substorm along with westward electrojet. Image of CNA also shows the localized enhancement during the onset

Figure 2. Observation at Maitri during 17–20 March 2015. (first to third rows) The variation in *H*, *D*, and *Z* components. (fourth row) The CNA data of imaging riometer with wide beam application. (fifth row) The image of CNA with narrow beam application.

of storm (refer to Figure 2). Absorption is patchy in nature and does not cover the full field of view (FOV) of the imaging riometer. However, pronounced CNA is observed during the intensification of westward electro-jet centered at 17 March midnight. The maximum value of CNA obtained is ~2.1 dB during the same hours. Multiple CNA onset spikes along with background CNA enhancements are also observed. Probably, these spikes in CNA image are direct field line precipitation of electrons in the nightside during substorm activity. Finally, CNA came to its minimum value at 0800 UT. Thereafter, again, CNA level rose, but there was absence of any westward electrojet. During 15–18 UT, a sudden CNA enhancement is observed which is equally strong ~2.2 dB as the maximum CNA enhancement during the main phase of the geomagnetic storm and this anomaly forms one of the main focuses of the current study. Instead of westward electrojet, occurrence of eastward electrojet at Maitri *H* component variation data during the period is evident as shown in Figure 2 (first row). The occurrences of eastward electrojet is discussed in great details in the section 3.3. Further, we did not observe any such huge enhancement in the CNA level throughout the recovery phase as occurred during 15–18 UT of 18 March.

For further examination, we have filtered the CNA and *H* component data in the Pc5 band (2–7 mHz) of 18 March 2015 and presented in Figure 3. Butterworth filter with sixth-order band pass in the frequency range of 2–7 mHz has been used for the filtering process. Figure 3 (first row) shows the *AU* and *AL* indices. Figure 3 (second and third rows) shows filtered data of *H* variation followed by filtered CNA data. To compare the onset of CNA and related Pc5 wave power, wide beam CNA data have been plotted in Figure 3 (fourth row). It can be seen that Pc5 wave in geomagnetic data is present throughout the day, but with multiple bursts of different amplitudes. Also, we see multiple burst of pulsations in the CNA data in Pc5 range. However, it discon-tinues unlike geomagnetic pulsations; for example, no pulsation activity can be seen during 0600–0900 UT and 1800–2200 UT. The correlation is very poor (correlation coefficient, *R* < 0.2) between the Pc5 structure in geomagnetic field and CNA. Interestingly, only those time sector had no Pc5 activity in the CNA where CNA was at its minimum level, or it can be seen that pulsations in the CNA is well evident during enhance-ment of CNA throughout the day. Hence, we suspect the possible relation between the pulsation activity in CNA and the level of CNA enhancement. Additionally, it is seen that the largest and prolonged Pc5 burst in the CNA data occurred during 1500–1800 UT. We also observed burst in the geomagnetic pulsation during this period. Among geomagnetic Pc5 bursts during 18 March 2015, the strongest burst was observed during 2100–2400 UT, but with soft CNA pulsations. The reason for small amplitude pulsation in CNA may be due to not so large occurrences of CNA during this period.
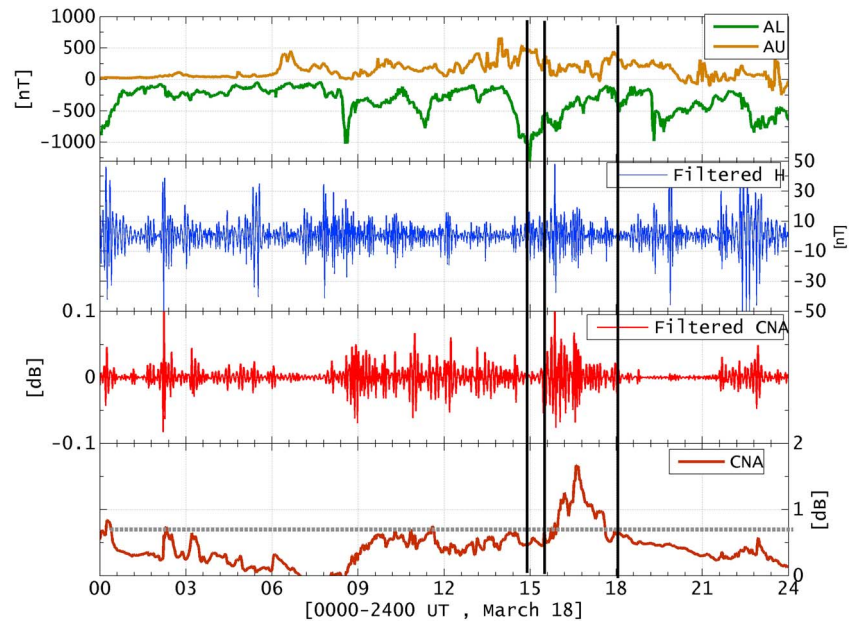
Figure 3. (second and third rows) The filtered *H* and CNA data in the Pc5 band (2–7 mHz) during 18 March 2015. (fourth row) The wide beam CNA data. (first row) *AL* index has been plotted to show the delay between substorm onset and CNA onset.

3.3. Magnetic Field Variation at Different Latitudes and Longitudes

The IMAGE chain stations are precisely meant to monitor the auroral electrojet dynamics within and around the standard auroral oval. It covers a geographical latitudinal range of 54–79°N. Figure 4 depicts the *H* variations during 18 March 2015 at the IMAGE chain stations in the narrow longitude range of 102–106°E with decreasing latitudes from top to bottom panel along with filtered data in the Pc5 band (2–7 mHz) at their rightside, respectively. The details of the stations are given in Table 1. Figure 4 (left column) clearly shows that
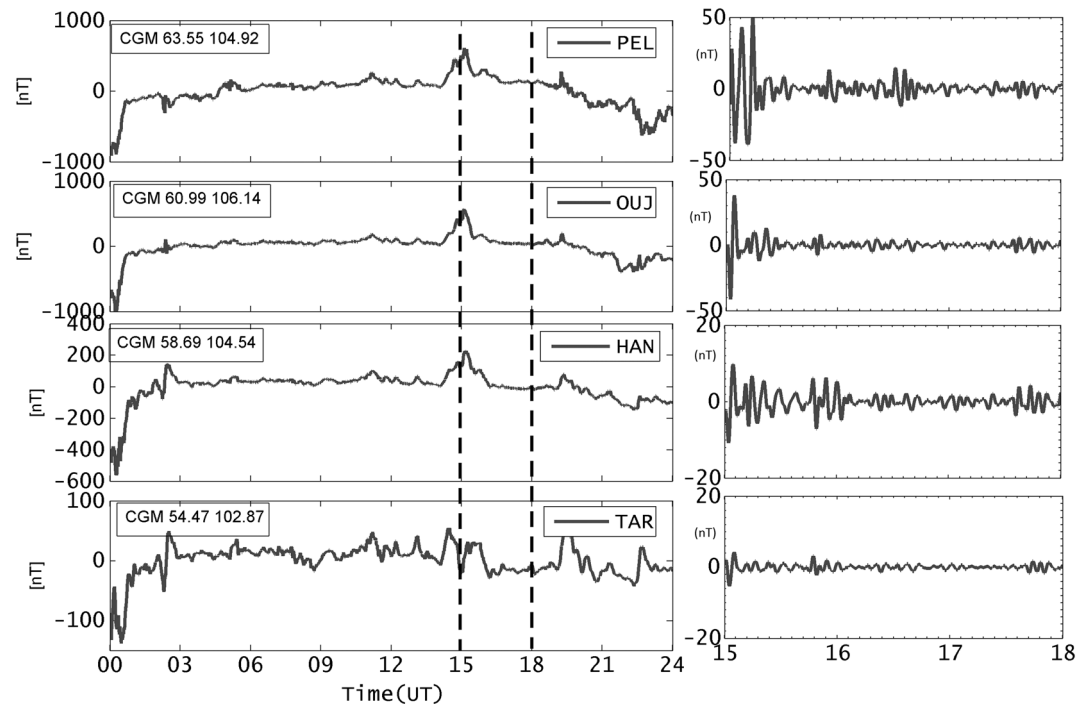

Figure 4. (left column) The *H* variation at different IMAGE chain stations with decreasing order of latitudes from top to bottom. (right column) The filtered data in Pc5 band (2–7 mHz) of Figure 4 (left column).

Table 1. Geographic and Geomagnetic Coordinates of the IMAGE Stations Used in the Present Study

Sr. No.	Stations	Geographic Latitude (°N)	Geographic Longitude (°E)	CGM Latitude (°N)	CGM Longitude (°E)
1	PEL	66	24	63	104
2	OUJ	64	27	60	106
3	HAN	62	26	58	104
4	TAR	58	26	54	102

no signatures of any electrojet is seen after 0300 UT up to 1400 UT. However, the presence of eastward electrojet is clearly marked at the stations PEL, OUJ, and HAN ∼1400 UT onward with decrease in intensity at lower latitudes. For example, PEL shows of maximum intensity of ∼500 nT, whereas TAR shows an intensity of only ∼30 nT. This suggests that the onset location of the substorm is within the auroral oval. In other words, substorm onset might have occurred near PEL station which has the same latitude as that of Maitri station. The interval marked by dashed lines indicate a time period of 03 h when huge precipitation has taken place at Maitri. Hence, we would expect the presence of direct precipitation at the location of Maitri during this time period. Figure 4 (right column) shows that wave power of Pc5 pulsations decrease with decreasing latitudes. No clear signature of Pc5 waves are seen at TAR station compared to other higher latitudinal stations.

The presence of eastward electrojet at Maitri is shown in Figure 5 and discussed further. Figure 5 depicts the *H* variation at the longitudinally distributed stations (shown in Table 2) with similar latitude as Maitri in order to examine the characteristics of eastward electrojet longitudinally during 1500 UT to 1800 UT. Clear simultaneous onsets of eastward electrojet at stations SOD, PEL, JCK, and DON are evident. The onset time is ∼1400 UT at SOD . However, a delay of ∼1 h is seen at Maitri. Since Maitri is away from local midnight sector and more eastward, this results in the delay onset of eastward electrojet at Maitri. Additionally, the intensity
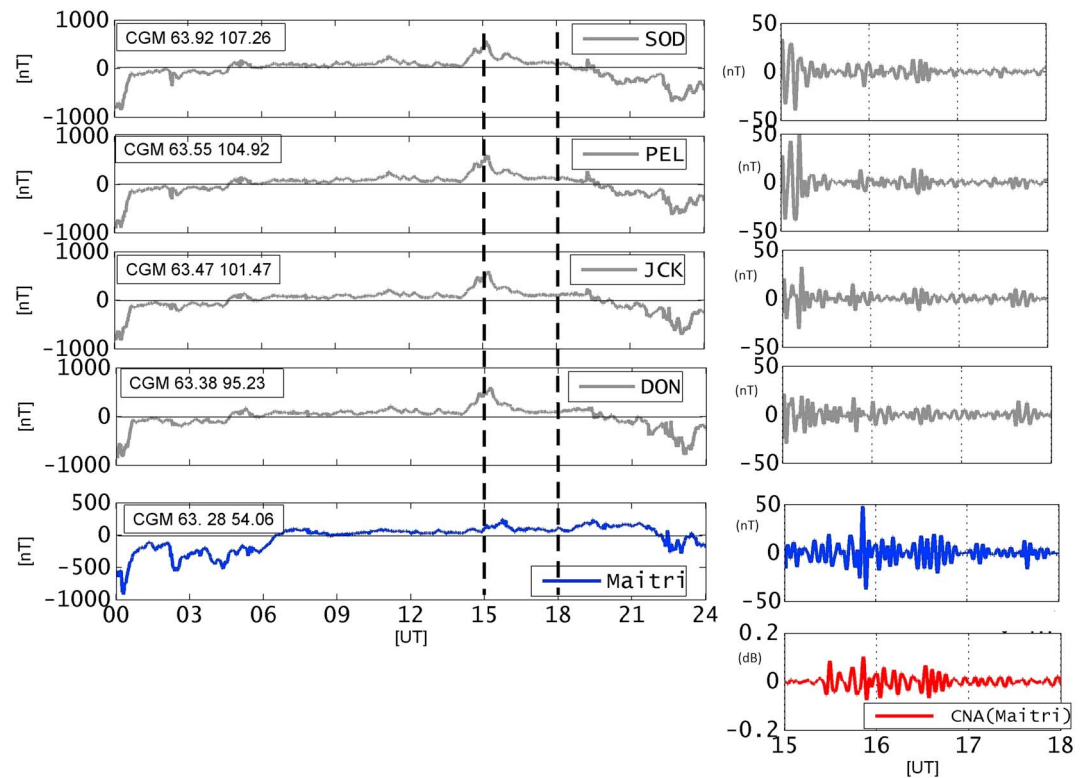

Figure 5. (left column) The *H* variation at different IMAGE chain stations including Maitri station with decreasing order of longitudes (Maitri is shown in blue color) from top to bottom; (right column) the filtered data in Pc5 (2–7 mHz) band of Figure 5 (left column). Again, Maitri is shown in blue color. Additionally, CNA data at Maitri filtered at Pc5 band have been shown in the red color at the bottom panel of Figure 5 (right column).

Table 2. Geographic and Geomagnetic Coordinates of the IMAGE Stations Having Latitude Similar to Maitri

Sr. No.	Stations	Geographic Latitude (°N)	Geographic Longitude (°E)	CGM Latitude (°N)	CGM Longitude (°E)
1	SOD	67	26	63	107
2	PEL	66	24	63	104
3	JCK	66	16	63	101
4	DON	66	12	63	95
5	MAI	−70	11	−63	54

of the eastward electrojet reduced with its longitudinal propagation. Figure 5 (right column) shows the filtered H variations in the Pc5 band (similar to Figure 4) for the respective left column stations. H variation and filtered H variation data for Maitri have been colored in blue and filtered CNA data for Maitri with red for the duration of 1500–1800 UT. It is evident that geomagnetic and CNA pulsations occurred simultaneous at Maitri, whereas no other station of IMAGE chain showed similar Pc5 burst around that interval (1500–1800 UT). In Figure 3, it was already seen that CNA pulsations are most pronounced during this interval. Hence, it is localized to Maitri. Figure 6 depicts the dynamic spectrum of filtered H variation and CNA in the Pc5 band during 15–18 UT, respectively. Frequency range 2–3 mHz is seen to be present in both spectra. However, dominance of these frequencies are not throughout the time series. For example, dynamic spectrum of filtered H component shows clear presence of 2–3 mHz frequency range during 1530–1600 UT, whereas dynamic spectrum of CNA shows the presence of similar frequencies at 1530–1630 UT. Nevertheless, both the time series show the dominance frequency range of 2–3 mHz.

3.4. Wave-Particle Interactions: VLF or EMIC?

The production of large CNA during afternoon sector at Maitri and its possible cause are the central themes of this study. Many literature have suggested that precipitation and related CNA enhancement at high latitude particularly at $4 < L < 7$ during storm time substorm is possible due to direct field line precipitation of approximately keV electrons restricted to midnight sectors. Also, wave-particle interactions between VLF waves and subrelativistic electrons can scatter charge particles and subsequently lead to the precipitations as shown previously. Ion cyclotron (EMIC) waves are also potential candidates for scattering the relativistic electrons and subsequent precipitation of those [*Rodger et al.*, 2008; *Miyoshi et al.*, 2008], and hence, it can also be the cause of such large afternoon CNA at Maitri. Basically, the whistler mode chorus waves are observed in the dawn sector with series of short rising tones in the frequency band of ∼1–2.5 kHz. These specific structured chorus waves occur predominantly outside the plasmapause ($L > 5$). Chorus can drive energetic electron precipitation [*Tsurutani and Lakhina*, 1997; *Pasmanik and Trakhtengerts*, 1999; *Trakhtengerts and Rycroft*, 2008;
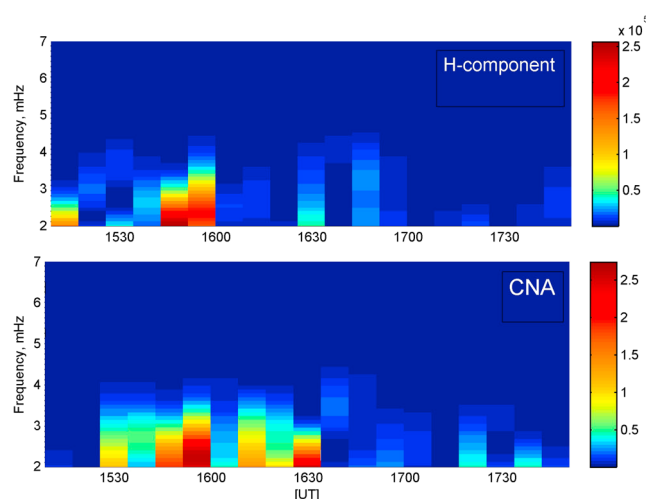

Figure 6. Dynamics spectrum of filtered (2–7 mHz) H component and CNA data at Maitri, Antarctica, during 1500–1800 UT of 18 March.

Bortnik and Thorne, 2007; *Gołkowski and Inan*, 2008] facilitated by the electron-cyclotron resonance and pitch angle diffusion. Therefore, the radiation belt energetic electrons may get precipitated by these chorus waves to the high-latitude ionosphere [*Tsurutani and Lakhina*, 1997; *Lorentzen et al.*, 2001; *Meredith et al.*, 2001; *Summers*, 2005]. These energetic electrons may penetrate down to the lower part of the ionosphere (D region) resulting in significant CNA. The chorus emission is seen to occur simultaneously with the onset of substorm [*Tsurutani and Smith*, 1974; *Anderson and Maeda*, 1977]. Plasmaspheric hiss, additionally, are also considered as potential cause of particle precipitation. Generally, these hiss
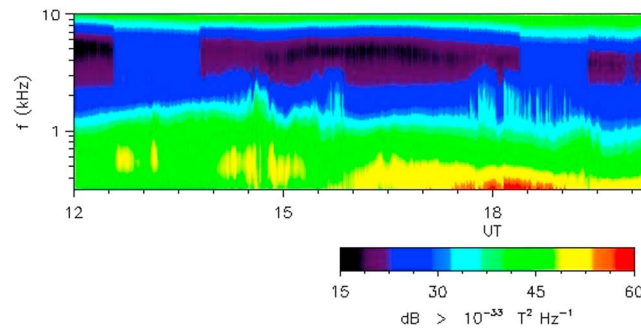
Figure 7. Dynamic spectrum of VLF data from Halley (75.58°S, 26.233°W) for the duration of 1200–2030 UT on 18 March 2015 is shown here.

waves occur inside the plasmasphere. However, they can be significantly stronger during geomagnetic substorms [*Smith et al.*, 1974; *Thorne et al.*, 1974]. These plasmaspheric hiss can also scatter the energetic electrons into the loss cone [*Titova et al.*, 1997; *Summers et al.*, 2008; *Yuan et al.*, 2012]. Plasmaspheric hiss are, in general, different from chorus because of their structureless occurrence in the ELF band (300 Hz to several kilohertz). Moreover, there are 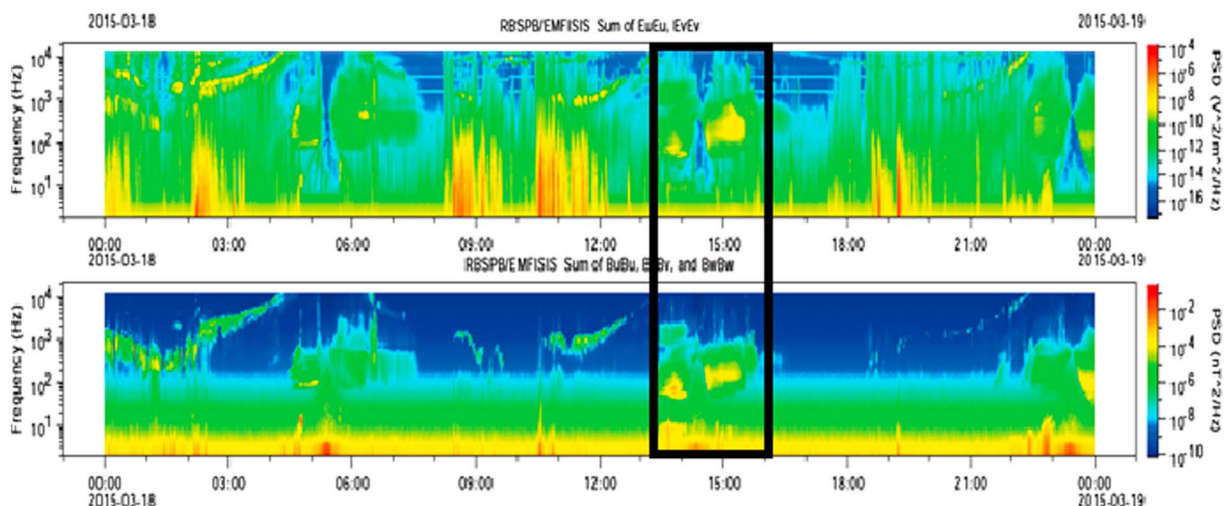many studies which show the possible occurrences of hiss-like waves in detached high-density plasma regions outside the typical plasmasphere, mostly in the dusk-evening sector [*Chan and Holzer*, 1976; *Cornilleau-Wehrlin et al.*, 1978]. More recently, *Tsurutani et al.* [2015] has done a detailed study on the hiss occurrences and have shown that they are predominantly present at *L* value 3–6 in the dusk sector (15–21 MLT) and the hiss generation in this limited region was attributed to ~10–100 keV electrons which drifted into this plasmaspheric bulge region. Here we have tried to examine all sort of possibilities, which could lead to the precipitation and related CNA enhancement during 1500–1800 UT on 18 March 2015. Figure 7 is showing the dynamic spectrum of VLF signal strength from Halley station(75.58°S, 26.233°W) for the duration of 1200–2030 UT on 18 March 2015. Halley station is nearer to Maitri in terms of geographic as well as CGM latitude but has different longitudes. It is ~2 h west to the Maitri station. The dynamic spectrum of VLF data clearly shows the presence of hiss during the period of 1500–1800 UT when large CNA has occurred at Maitri. Since then, the *L* value of Maitri is 5 and time occurrences of large CNA during 1400–1800 may be due to scatting of electrons in the plasma bulge region. The first hiss burst can be seen during 1400–1530 UT as yellow patch with ~50 dB intensity, later continuous occurrence of hiss can be seen up to 1800 UT. The first hiss burst fall within the frequency range of ~300–800 Hz and the latter one fall in between ~100 and 600 Hz. Several bursts can be seen above 1 KHz. However, they cannot be termed as chorus as they do not have any consistent structures as shown by *Manninen et al.* [2010]. Also, observation of VLF chorus-related precipitation during afternoon hours is not so common. Interestingly, during afternoon hours and late evening hours, precipitation due to EMIC wave is literally evident. Hence, we also have examined the presence of EMIC wave at Maitri. However, we do not see any EMIC wave presence during these hours. Additionally, Figure 4 clearly shows the presence of eastward electrojet at Maitri during 1500–1800 UT. Hence, we presume these two processes viz., (1) VLF scattered subrelativistic electron precipitation in the presence of ULF wave and (2) direct field line precipitation seen

Figure 8. Top panel and bottom panel show DSP of electric field and magnetic field, respectively, obtained from RBSP-B satellite. Occurrence of hiss waves is highlighted with the help of a black box.
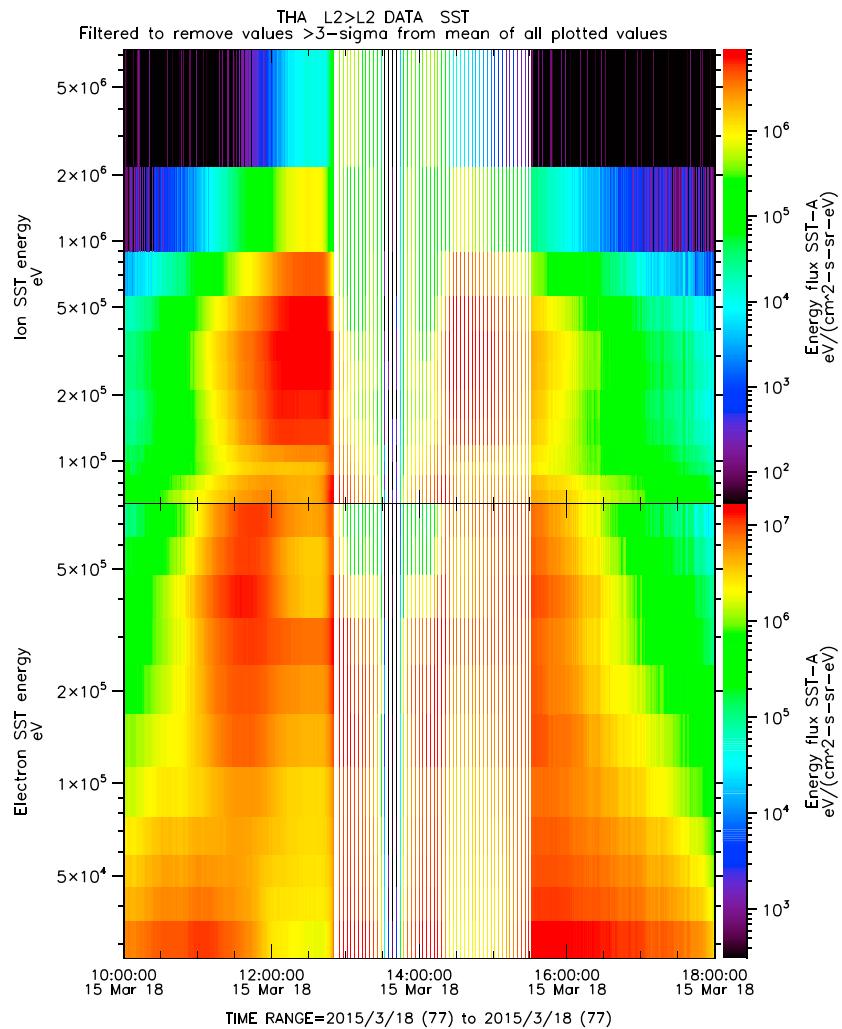
Figure 9. Electron and ion energy eflux spectrum for the duration of 1000–1800 UT of 18 March 2015. The presence of huge electrons in the energy band of hundreds of keV is clearly evident.

as eastward electrojet together might have produced such huge CNA in the afternoon hours at Maitri. In order to get in situ observation of wave activities at inner magnetosphere region which maps down to $L = 5$ during the dusk hours, a survey of satellites was done. It is observed that RBSP-A, RBSP-B, THEMIS-A (P5), and THEMIS-D (P3) were orbiting in the favorable L values. One can track their orbits by utilizing 4-D Orbit Viewer provided by NASA. However, observation of RBSP-A was neglected as it was approaching dawn during the event hours. Fortunately, RBSP-B was passing the dusk hours within the plasmapause for a very small period of time (~90 min) between 1400 and 1500 UT. Figure 8 is showing the PSD of electric field in the top panel and PSD of magnetic field in the bottom panel. These plots were collected from EMFISIS summary plots. Interestingly, clear presence of hiss waves can be seen in both panels highlighted within a black box. The occurrences of these hiss waves exactly matches the time when the satellite was within the plasmapause during dusk hours. Figure 9 is presenting the electron and ion energy eflux spectrogram from THEMIS-A (P5), where it is clearly seen that huge population of electron flux in the hundreds of keV range. THEMIS-D (P3 also showed similar enhancement of electron energy flux during the event period (figure is not shown)).

4. Transfer Entropy Method to Evaluate the Cause and Effect Relation Between Geomagnetic and CNA Pulsations

The geomagnetic pulsations were present almost throughout during the first recovery phase day, whereas CNA pulsations were seen to be present during high production of CNA on 18 March 2015. That simply
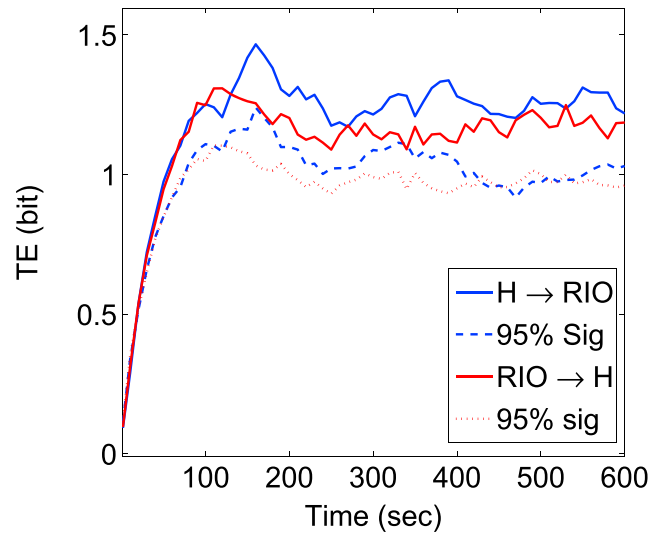
Figure 10. Transfer entropy between two time series, i.e., *H* and CNA data of Maitri for the duration of 1500–1800 UT of 18 March 2015.

describes disturbed plasma system which might have been modulated by the field line oscillations [*Pilipenko*, 1990]. However, *Sato and Matsudo* [1986] have shown that the geomagnetic pulsation modulating CNA pulsation are not always true. In order to find the cause and the effect in these two pulsations, we have adopted a novel technique called transfer entropy method.

Schreiber [2000] introduced transfer entropy (TE) method which quantifies the information exchanged between any two variables [*Schreiber*, 2000; *De Michelis et al.*, 2011]. This exchange of information essentially has direction with no bearing on their common history or inputs, unlike cross correlation. Therefore, it can be utilized for determining the cause and effect relationship between two variables [*Das Sharma et al.*, 2012; *Vichare et al.*, 2016]. Transfer entropy between two random variables or processes *x* and *y* is mathematically represented as

$$\text{TE}_{x \to y}(\tau) = \sum P(y(t+\tau), y(t), x(t)) \log_2 \left(\frac{P(y(t+\tau), y(t), x(t)) * P(y(t))}{P(x(t), y(t)) * P(y(t+\tau), y(t))} \right) \tag{1}$$

where P(y(t + s), x(t)) is the joint probability of y(t + s) and x(t) and P(y(t + τ), y(t), x(t)) is the joint probability of y (t + τ), y (t) and x (t).

More details of this technique can be found in *Vichare et al.* [2016]. Here TE is applied to establish the driver and response from the pair, geomagnetic pulsations observed in magnetometer and CNA data. Note that CNA acts as a good proxy for the particle precipitation and *H* component is a good proxy for geomagnetic field line oscillations. Both data sets show the periodic variations within Pc5 band, which posed the question who drives whom?

The filtered time series of CNA recorded in imaging riometer and *H* component of geomagnetic field at Maitri of time window 1500–1800 UT on 18 March are considered to compute transfer entropy (TE). As data are filtered, the resultant time series are stationary in nature and TE can be applied. Data were downsampled to 10 s resolution. TE is computed in both directions, i.e., from geomagnetic pulsation to pulsation observed in CNA and vice versa. The significance level is estimated by following surrogate data test [*Theiler et al.*, 1992]. The TE values are shown in Figure 10 with significance level. Estimated TE values are statistically significant. Figure 10 clearly shows that there is maximum information flow observed from *H* → RIO at time lag ~160 s, and for most of the time lags the TE values for *H* → CNA are higher compared to CNA → *H*. This implies that there is a net information flow from *H* → CNA. Thus, transfer entropy technique used has indicated that geomagnetic pulsation modulates particle precipitation observed at the station during the early recovery phase of St. Patrick's storm of 2015.

5. Discussion

It is the first observation of pronounced CNA production along with simultaneous geomagnetic pulsation and CNA pulsation at Indian Antarctic station, Maitri, during the early recovery phase of 2015 St. Patrick's Day geomagnetic storm. Maitri ($L = 5$; CGM 62°S, 55°E) is situated at the lower fringe of auroral oval (CGM 65–75°), and its ionosphere only responds to moderate to intense substorms. Mainly storm time substorm are able to alter the state of ionosphere over Maitri, Antarctica [*Behera et al.*, 2015]. Interestingly during the largest geomagnetic storm of this current solar cycle, it is observed that the production of CNA at high latitude during the recovery phase can be as large as that of the CNA during the main phase of the storm. Our interest lies in the time window of 1500–1800 UT on 18 March 2015 (first day of the recovery phase) wherein the CNA enhancement was as larger as the maximum CNA production during main phase of the St. Patrick's storm. Additionally, we observe the presence of geomagnetic pulsations and pulsations in CNA during 18 March 2015. Pulsations with larger wave power and longer duration coincided with the largest production of CNA during 1500–1800 UT.

Even though the interplanetary conditions were quite steady and less dynamic compared to the main phase, the interplanetary parameter such as solar wind (V_s), IMF B_z and corresponding eastward component of interplanetary electric field (IEF) E_y were significant during the period of 1500–1800 UT. The strongest substorm appeared during this period with maximum excursion in AL index of ~ -1300 nT. The solar wind parameters such as IMF B_z (~ -10 nT) and V_s (~ 600 km/s) were comparatively large during this period. The other parameters such as solar wind density and dynamics pressure showed some enhancement compared to other sector of the day (18 March), though these values were pretty low compared to their values during the main phase of the storm.

The enhancement of CNA during afternoon sector might be the result of simultaneously occurring three major processes causing particle precipitation. First is the precipitation of electrons which set up the field-aligned current and arises due to the disruption of tail current. Second, precipitation could be possible due to the interaction of plasmaspheric hiss with eastward propagating subrelativistic electron flux. Third, EMIC might also scatter relativistic electrons and ions and allow them to fall into the loss cone to enhance precipitation at high-latitude ionosphere. Many researcher have shown that EMIC-related scattering are notable during dusk hours within L value less than 5. Considering the location of Maitri and MLT of the event, we first examined the third possibility. During the period of interest, Maitri ($L \sim 5$) is in dusk sector. So we expect the presence of EMIC waves. Pc1 and Pc2 in the ground magnetometers are the signature of EMIC waves. Data from induction coil magnetometer were used to examine the presence of EMIC waves (figures are not shown). However, we did not see any signature of EMIC waves. Hence, the contribution from EMIC-driven precipitation can be discarded in the present case. Second process seems to be the main source of precipitation. The presence of plasmaspheric hiss is evident during 1500–1800 UT at Halley station which is having the same latitude as Maitri station. The dynamic spectrum of VLF signal showed multiple bursts within 1 kHz. Structureless patches confirm the occurrence of hiss, not chorus which is rare at $L = 5$ during afternoon hours. [*Behera et al.*, 2016] have shown that precipitation of particle at the day side can occur due to pitch angle scattering of subrelativistic electrons, especially in the prenoon sector. Nevertheless, the criteria that adopted in *Behera et al.* [2016] have been followed in order to examine whether this is also a case of such day side CNA event or not. There are two most important things viz., absence of westward electrojet over Maitri during substorm activity and a certain delay between the onset of substorm as observed in AL index and onset of CNA at Maitri qualify a CNA event to be called as a dayside CNA event at Maitri. Apparently, it is found that the event satisfies the criteria for the dayside CNA. Here susbtorm activity is observed prior to the onset of CNA with a time delay of ~ 60 min. This time delay has been fitted in the gradient curvature equation [*Beharrell et al.*, 2015] in order to estimate the energy range of the electron flux resulting into large CNA at Maitri. No westward electrojet signature was evident during the event. Hence, similar exercise was carried out as mentioned in [*Behera et al.*, 2016]. The estimated energy range is found to be 150–350 keV. Figure 11 is showing the electron flux of 40–475 keV energy band observed in GOES 15 and GOES 13 satellites for 18 March 2015. Since both satellites were far in LT from the CNA observation site (Maitri), we estimated the percentage residual flux, which could reach to Maitri. From the comparative observations at both satellites, it was found that loss rate is found to be 0.33% per degree in the 150 keV band and 0.16% per degree in the 275 keV band. Hence, approximately 40% and 60% of flux will reach to Maitri during the event in the energy band of 150 keV and 275 keV, respectively. There were three major burst of electron flux occurred at ~ 0820 UT, ~ 1140 UT, and ~ 1510 UT, respectively. Interestingly, all these three bursts relate to three major substorm onsets. Out of three substorms, the substorm that occurs
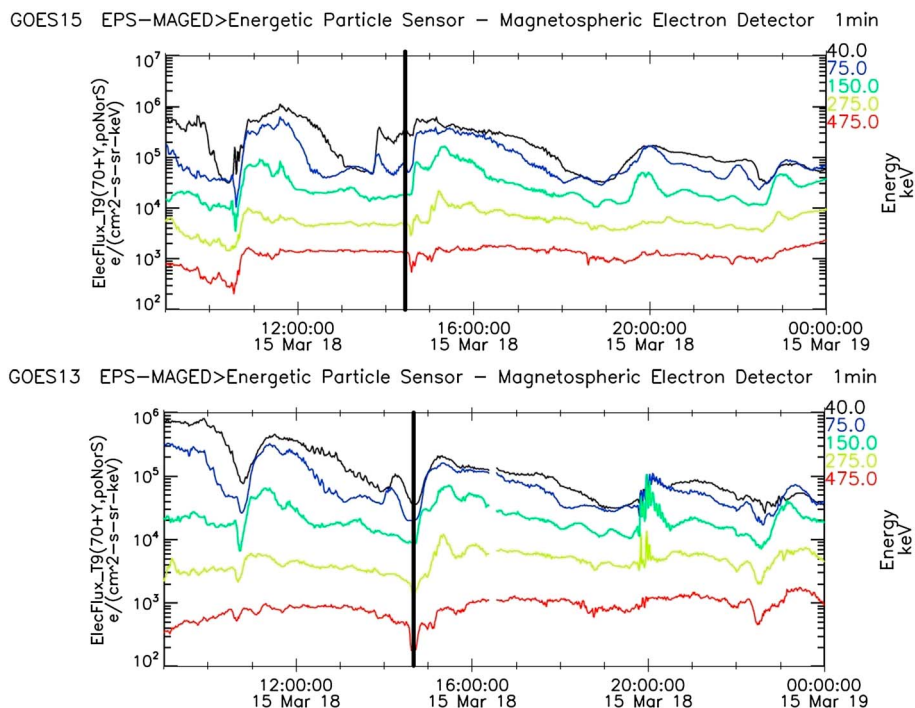
Figure 11. The 1 min resolution data of 40–475 KeV electron flux densities by GOES 13 and GOES 15 during 18 March 2015.

~1410 UT onward was most intense but with comparatively less flux enhancement as shown in Figure 11 and with highest CNA enhancement (refer to Figure 3). This allow us to think of an additional factor that might help in producing such huge CNA during 15–18 UT. Nevertheless, enhancement of electron fluxes are seen in the energy range of 75–275 keV which agreed with the assumption that made by gradient-curvature drift calculation. Hence, it can be assumed that plasmaspheric hiss as observed at Halley station (please refer to section 3.4) and enhanced flow of eastward propagating keV electrons might have undergone wave-particle interactions causing primarily such huge CNA at Maitri.

The presence of eastward electrojet during the period of our interest is expected to be the additional contributing factor for such CNA enhancement during 1500–1800 UT of 18 March at Maitri. Figure 5 clearly shows the presence of eastward electrojet at Maitri during 1500–1800 UT. Signatures of eastward electrojet was visible longitudinally with certain time delay in the IMAGE chain stations with latitude close to Maitri. Stations such as SOD, PEL, KCK, and DON are longitudinally close enough and hence visible delay between the onset of eastward electrojet was not observed. Nevertheless, visible delay appeared at Maitri as that is far and westward to other stations shown in the Figure 5. Presence of eastward electrojet was quite evident with $\Delta H \sim 250$ nT. Eastward electrojet is mainly driven by reconnection as suggested by a statistical study with an empirical ionospheric model performed by *Gjerlov and Hoffman* [2001]. Therefore, we presume that the presence of eastward electrojet may be an additional factor for such huge CNA at Maitri during postnoon sector.

Additionally, the presence of strong geomagnetic Pc5 pulsation is evident at the stations nearer to Maitri and other station nearer to auroral latitudes than the equatorward stations. Also, CNA pulsation was seen at Maitri along with geomagnetic pulsation predominantly ~2–3 mHz range during the same hour of enhanced CNA (please see Figure 3). This has created confusion to understand the cause and effect relationship between the geomagnetic and CNA pulsation. To identify the cause and effect relationship between the geomagnetic pulsation and CNA pulsation at Maitri, a novel approach, i.e., transfer entropy (TE) method, was used, which confirms the modulation of cosmic noise absorption due to the geomagnetic pulsations (discussion in section 4).

In situ observation from RBSP-B clearly shows the presence of hiss waves in the range of hundreds of hertz, maximized at 300 Hz, thereby supporting our inference. The clear indication of hiss waves presence

as observed by RBSP-B and huge population of hundreds of keV electron flux as observed from THEMIS-A allow us to think of wave-particle interaction between the hiss waves and hundreds of keV electrons that have given rise to huge CNA at Maitri.

6. Conclusions

The current study attempts to understand the sudden rise in CNA level during the recovery phase particularly at 1500–1800 UT of the largest geomagnetic storm of the current solar cycle and lead to the following key points:

1. The CNA enhancement in the early recovery phase, particularly in the afternoon sector (1500–1800 UT) at Maitri ($L = 5$) was as large as that during main phase CNA. The location of Maitri is indeed situated well within the plasma bulge region where maximum precipitation of energetic electrons were expected due to hiss waves.
2. Absence of electromagnetic ion cyclotron (EMIC) waves has pointed the role of VLF in production of such huge CNA during the afternoon hours at Maitri ($L = 5$). However, VLF observation from the Halley station (75.58°S, 26.233°W) shows the presence of hiss instead of chorus with multiple bursts during 1500–1800 UT. Nevertheless, in situ observation of hiss waves clearly in PSD of electric field and magnetic field data from RBSP-B support the inference. Essentially, Halley station was also inside the plasma bulge region.
3. Hence, it can be considered that hiss and enhanced flow of eastward propagating hundreds of keV electrons as observed by GOES 15 and GOES 13 might have undergone wave-particle interactions causing primarily such huge CNA at Maitri. The observation is completely in agreement with the statistical study of plasmaspheric hiss by *Tsurutani et al.* [2015].
4. Moreover, simultaneity of CNA pulsations with geomagnetic pulsations during the same hours is also evident in the frequency range of 2–3 mHz.

Finally, it can be concluded that production of large CNA was possible due to simultaneously occurring two processes viz., (1) field line precipitation which was evident from the presence of eastward electrojet and (2) scattering of subrealtivistic electrons by hiss waves inside the plasma bulge region in spite of VLF chorus. And the pulsation in CNA is caused by geomagnetic pulsations in this event.

References

Anderson, B. J., R. E. Erlandson, and L. J. Zanetti (1992), A statistical study of Pc 12 magnetic pulsations in the equatorial magnetosphere: 1. Equatorial occurrence distributions, *J. Geophys. Res.*, *97*(A3), 3075–3088, doi:10.1029/91JA02706.

Anderson, R. R., and K. Maeda (1977), VLF emissions associated with enhanced magnetospheric electrons, *J. Geophys. Res.*, *82*(1), 135–146.

Ansari, Z. (1964), The aurorally associated absorption of cosmic noise at college, Alaska, *J. Geophys. Res.*, *69*(21), 4493–4513.

Astafyeva, E., I. Zakharenkova, and M. Förster (2015), Ionospheric response to the 2015 St. Patrick's Day storm: A global multi-instrumental overview, *J. Geophys. Res. Space Physics*, *120*, 9023–9037, doi:10.1002/2015JA021629.

Baker, G. J., E. F. Donovan, and B. J. Jackel (2003), A comprehensive survey of auroral latitude Pc5 pulsation characteristics, *J. Geophys. Res.*, *108*, 1384, doi:10.1029/2002JA009801.

Beharrell, M., F. Honary, C. J. Rodger, and M. A. Clilverd (2015), Substorm-induced energetic electron precipitation: Morphology and prediction, *J. Geophys. Res. Space Physics*, *120*, 2993–3008, doi:10.1002/2014JA020632.

Behera, J. K., A. K. Sinha, A. K. Singh, G. Vichare, A. Dhar, S. Labde, and K. Jeeva (2015), Substorm related CNA near equatorward boundary of the auroral oval in relation to interplanetary conditions, *Adv. Space Res.*, *56*(1), 28–37.

Behera, J. K., A. K. Sinha, G. Vichare, O. Kozyreva, R. Rawat, and A. Dhar (2016), Dayside cosmic noise absorption at the equatorward boundary of auroral oval as observed from Maitri, Antarctica ($L = 5$; CGM 62.45°S, 55.45°E), *J. Geophys. Res. Space Physics*, *121*, 3198–3211, doi:10.1002/2016JA022418.

Bortnik, J., and R. Thorne (2007), The dual role of ELF/VLF chorus waves in the acceleration and precipitation of radiation belt electrons, *J. Atmos. Sol. Terr. Phys.*, *69*(3), 378–386.

Chan, K.-W., and R. E. Holzer (1976), ELF hiss associated with plasma density enhancements in the outer magnetosphere, *J. Geophys. Res.*, *81*(13), 2267–2274.

Cherniak, I., and I. Zakharenkova (2015), Dependence of the high-latitude plasma irregularities on the auroral activity indices: A case study of 17 March 2015 geomagnetic storm, *Earth Planets Space*, *67*(1), 151.

Cornilleau-Wehrlin, N., R. Gendrin, F. Lefeuvre, M. Parrot, R. Grard, D. Jones, A. Bahnsen, E. Ungstrup, and W. Gibbons (1978), VLF electromagnetic waves observed onboard GEOS-1, *Space Sci. Rev.*, *22*(4), 371–382.

Criswell, D. R. (1969), Pc 1 micropulsation activity and magnetospheric amplification of 0.2-to 5.0-Hz hydromagnetic waves, *J. Geophys. Res.*, *74*(1), 205–224.

Das Sharma, S., D. Ramesh, C. Bapanayya, and P. Raju (2012), Sea surface temperatures in cooler climate stages bear more similarity with atmospheric CO_2 forcing, *J. Geophys. Res.*, *117*, D13110, doi:10.1029/2012JD017725.

De Michelis, P., G. Consolini, M. Materassi, and R. Tozzi (2011), An information theory approach to the storm-substorm relationship, *J. Geophys. Res.*, *116*, A08225, doi:10.1029/2011JA016535.

Detrick, D., and T. Rosenberg (1990), A phased-array radiowave imager for studies of cosmic noise absorption, *Radio Sci.*, *25*(4), 325–338.

Gjerloev, J. W., and R. A. Hoffman (2001), The convection electric field in auroral substorms, *J. Geophys. Res.*, *106*, 12,919–12,931, doi:10.1029/1999JA000240.

Gołkowski, M., and U. S. Inan (2008), Multistation observations of ELF/VLF whistler mode chorus, *J. Geophys. Res.*, *113*, A08210, doi:10.1029/2007JA012977.

Honary, F., S. R. Marple, K. Barratt, P. Chapman, M. Grill, and E. Nielsen (2011), Invited article: Digital beam-forming imaging riometer systems, *Rev. Sci. Instrum.*, *82*(3), 031301.

Iijima, A. K., A. Saito, W. Gonzalez, and F. Guarnieri (2005), Dayside global ionospheric response to the major interplanetary events, *Geophys. Res. Lett.*, *32*, L12S02, doi:10.1029/2004GL021467.

Kamide, Y., and K. Kusano (2015), No major solar flares but the largest geomagnetic storm in the present solar cycle, *Space Weather*, *13*(6), 365–367, doi:10.1002/2015SW001213.

Kawamura, M., M. Kuwashima, and T. Toya (1982), Comparative study of magnetic pc 1 pulsations observed at low and high latitudes: Source region and generation mechanism of periodic hydromagnetic emissions, *Mem. National Inst. Polar Res.*, *22*, 3–16.

Kennel, C. F., and H. Petschek (1966), Limit on stably trapped particle fluxes, *J. Geophys. Res.*, *71*(1), 1–28.

Kivelson, M. G., and P. Zu-Yin (1984), The Kelvin-Helmholtz instability on the magnetopause, *Planet. Space Sci.*, *32*(11), 1335–1341.

Li, H., Z. Yuan, X. Yu, S. Huang, D. Wang, Z. Wang, Z. Qiao, and J. R. Wygant (2015), The enhancement of cosmic radio noise absorption due to hiss-driven energetic electron precipitation during substorms, *J. Geophys. Res. Space Physics*, *120*, 5393–5407, doi:10.1002/2015JA021113.

Little, C. G., and H. Leinbach (1958), Some measurements of high-latitude ionospheric absorption using extraterrestrial radio waves, *Proc. IRE*, *46*(1), 334–348.

Little, C. G., and H. Leinbach (1959), The Riometer-A device for the continuous measurement of ionospheric absorption, *Proc. IRE*, *47*(2), 315–320.

Lorentzen, K., J. Blake, U. Inan, and J. Bortnik (2001), Observations of relativistic electron microbursts in association with VLF chorus, *J. Geophys. Res.*, *106*(A4), 6017–6027.

Manninen, J., N. Kleimenova, O. Kozyreva, and T. Turunen (2010), Pc5 geomagnetic pulsations, pulsating particle precipitation, and VLF chorus: Case study on 24 November 2006, *J. Geophys. Res.*, *115*, A00F14, doi:10.1029/2009JA014837.

Meredith, N. P., R. B. Horne, and R. R. Anderson (2001), Substorm dependence of chorus amplitudes: Implications for the acceleration of electrons to relativistic energies, *J. Geophys. Res.*, *106*(A7), 13,165–13,178.

Meredith, N. P., R. M. Thorne, R. B. Horne, D. Summers, B. J. Fraser, and R. R. Anderson (2003), Statistical analysis of relativistic electron energies for cyclotron resonance with EMIC waves observed on CRRES, *J. Geophys. Res.*, *108*, 1250, doi:10.1029/2002JA009700.

Miyoshi, Y., K. Sakaguchi, K. Shiokawa, D. Evans, J. Albert, M. Connors, and V. Jordanova (2008), Precipitation of radiation belt electrons by EMIC waves, observed from ground and space, *Geophys. Res. Lett.*, *35*, L23101, doi:10.1029/2008GL035727.

Nosé, M., et al. (2012), Wp index: A new substorm index derived from high-resolution geomagnetic field data at low latitude, *Space Weather*, *10*(8), S08002, doi:10.1029/2012SW000785.

Pasmanik, D., and V. Y. Trakhtengerts (1999), Spectral characteristics of waves and particles in the model of cyclotron wave-particle interactions near plasmapause, 17, 351–357

Pilipenko, V. (1990), ULF waves on the ground and in space, *J. Atmos. Terr. Phys.*, *52*(12), 1193–1209.

Pilipenko, V., O. Kozyreva, V. Belakhovsky, M. Engebretson, and M. Samsonov (2010), Generation of magnetic and particle Pc5 pulsations during the recovery phase of strong magnetic storms, *Proc. R. Soc. London, Ser. A*, *466*, 3363–3390.

Remya, B., B. Tsurutani, R. Reddy, G. Lakhina, and R. Hajra (2015), Electromagnetic cyclotron waves in the dayside subsolar outer magnetosphere generated by enhanced solar wind pressure: EMIC wave coherency, *J. Geophys. Res. Space Physics*, *120*(9), 7536–7551.

Rodger, C. J., T. Raita, M. A. Clilverd, A. Seppälä, S. Dietrich, N. R. Thomson, and T. Ulich (2008), Observations of relativistic electron precipitation from the radiation belts driven by EMIC waves, *Geophys. Res. Lett.*, *35*, L16106, doi:10.1029/2008GL034804.

Rodger, C. J., A. J. Kavanagh, M. A. Clilverd, and S. R. Marple (2013), Comparison between POES energetic electron precipitation observations and riometer absorptions: Implications for determining true precipitation fluxes, *J. Geophys. Res. Space Physics*, *118*, 7810–7821, doi:10.1002/2013JA019439.

Sato, N., and T. Matsudo (1986), Origin of magnetic pulsations associated with regular period VLF pulsations (type 2 QP) observed on the ground at Syowa station, *J. Geophys. Res.*, *91*(A10), 11,179–11,185.

Schreiber, T. (2000), Measuring information transfer, *Phys. Rev. Lett.*, *85*(2), 461–464.

Senior, A., and F. Honary (2003), Observations of the spatial structure of electron precipitation pulsations using an imaging riometer, *Ann. Geophys.*, *21*, 997–1003.

Seppälä, A., M. A. Clilverd, and C. J. Rodger (2007), NO_x enhancements in the middle atmosphere during 2003–2004 polar winter: Relative significance of solar proton events and the aurora as a source, *J. Geophys. Res.*, *112*, D23303, doi:10.1029/2006JD008326.

Singh, A. K., A. Sinha, R. Rawat, B. Jayashree, B. Pathan, and A. Dhar (2012), A broad climatology of very high latitude substorms, *Adv. Space Res.*, *50*(11), 1512–1523.

Smith, E., A. Frandsen, B. Tsurutani, R. Thorne, and K. Chan (1974), Plasmaspheric hiss intensity variations during magnetic storms, *J. Geophys. Res.*, *79*(16), 2507–2510.

Spanswick, E., E. Donovan, G. Baker (2003), Pc5 modulation of high energy electron precipitation: Particle interaction regions and scattering efficiency, *Ann. Geophys.*, *23*, 1533–1542.

Sripathi, S., S. Sreekumar, S. Banola, K. Emperumal, P. Tiwari, and B. S. Kumar (2015), Low-latitude ionosphere response to super geomagnetic storm of 17/18 March 2015: Results from a chain of ground-based observations over Indian sector, *J. Geophys. Res. Space Physics*, *120*, 10,864–10,882, doi:10.1002/2015JA021509.

Stauning, P. (1996), Investigations of ionospheric radio wave absorption processes using imaging riometer techniques, *J. Atmos. Terr. Phys.*, *58*(6), 753–764.

Summers, D. (2005), Quasi-linear diffusion coefficients for field-aligned electromagnetic waves with applications to the magnetosphere, *J. Geophys. Res.*, *110*, A08213, doi:10.1029/2005JA011159.

Summers, D., B. Ni, N. P. Meredith, R. B. Horne, R. M. Thorne, M. B. Moldwin, and R. R. Anderson (2008), Electron scattering by whistler-mode elf hiss in plasmaspheric plumes, *J. Geophys. Res.*, *113*, A04219, doi:10.1029/2007JA012678.

Theiler, J., S. Eubank, A. Longtin, B. Galdrikian, and J. D. Farmer (1992), Testing for nonlinearity in time series: The method of surrogate data, *Physica D*, *58*(1–4), 77–94.

Thomas, N., G. Vichare, A. Sinha, and R. Rawat (2015), Low-latitude Pi2 oscillations observed by polar Low Earth Orbiting satellite, *J. Geophys. Res. Space Physics*, *120*, 7838–7856, doi:10.1002/2014JA020958.

Thorne, R., E. Smith, K. Fiske, and S. Church (1974), Intensity variation of elf hiss and chorus during isolated substorms, *Geophys. Res. Lett.*, *1*(5), 193–196.

Titova, E. et al. (1997), Strong localized variations of the low-altitude energetic electron fluxes in the evening sector near the plasmapause, *Ann. Geophys.*, *16*, 25–33.

Trakhtengerts, V. Y., and M. J. Rycroft (2008), *Whistler and Alfven Mode Cyclotron Masers in Space*, Cambridge Univ. Press, Cambridge, U. K.

Tsurutani, B., E. Smith, H. West Jr., and R. Buck (1979), Chorus, energetic electrons and magnetospheric substorms, in *Wave Instabilities in Space Plasmas*, pp. 55–62, D. Reidel, Dordrecht, Netherlands.

Tsurutani, B., et al. (2004), Global dayside ionospheric uplift and enhancement associated with interplanetary electric fields, *J. Geophys. Res.*, *109*, A08302, doi:10.1029/2003JA010342.

Tsurutani, B., et al. (2016), Heliospheric plasma sheet (HPS) impingement onto the magnetosphere as a cause of relativistic electron dropouts (REDS) via coherent EMIC wave scattering with possible consequences for climate change mechanisms, *J. Geophys. Res. Space Physics*, *121*, 10,130–10,156, doi:10.1002/2016JA022499.

Tsurutani, B. T., and G. S. Lakhina (1997), Some basic concepts of wave-particle interactions in collisionless plasmas, *Rev. Geophys.*, *35*(4), 491–501.

Tsurutani, B. T., and E. J. Smith (1974), Postmidnight chorus: A substorm phenomenon, *J. Geophys. Res.*, *79*(1), 118–127.

Tsurutani, B. T., and E. J. Smith (1977), Two types of magnetospheric ELF chorus and their substorm dependences, *J. Geophys. Res.*, *82*(32), 5112–5128.

Tsurutani, B. T., G. S. Lakhina, and O. P. Verkhoglyadova (2013), Energetic electron (>10 keV) microburst precipitation, 5–15 s X-ray pulsations, chorus, and wave-particle interactions: A review, *J. Geophys. Res. Space Physics*, *118*, 2296–2312, doi:10.1002/jgra.50264.

Tsurutani, B. T., B. J. Falkowski, J. S. Pickett, O. Santolik, and G. S. Lakhina (2015), Plasmaspheric hiss properties: Observations from polar, *J. Geophys. Res. Space Physics*, *120*, 414–431, doi:10.1002/2014JA020518.

Tulasi Ram, S., et al. (2016), Duskside enhancement of equatorial zonal electric field response to convection electric fields during the St. Patrick's Day storm on 17 March 2015, *J. Geophys. Res. Space Physics*, *121*, 538–548, doi:10.1002/2015JA021932.

Turunen, E., P. T. Verronen, A. Seppälä, C. J. Rodger, M. A. Clilverd, J. Tamminen, C.-F. Enell, and T. Ulich (2009), Impact of different energies of precipitating particles on NO_x generation in the middle and upper atmosphere during geomagnetic storms, *J. Atmos. Sol. Terr. Phys.*, *71*(10), 1176–1189.

Verkhoglyadova, O. P., B. T. Tsurutani, A. J. Mannucci, M. G. Mlynczak, L. A. Hunt, L. J. Paxton, and A. Komjathy (2016), Solar wind driving of ionosphere-thermosphere responses in three storms near St. Patrick's Day in 2012, 2013, and 2015, *J. Geophys. Res. Space Physics*, *121*, 8900–8923, doi:10.1002/2016JA022883.

Viall, N., L. Kepko, and H. E. Spence (2009), Relative occurrence rates and connection of discrete frequency oscillations in the solar wind density and dayside magnetosphere, *J. Geophys. Res.*, *114*, A01201, doi:10.1029/2008JA013334.

Vichare, G., A. Bhaskar, and D. S. Ramesh (2016), Are the equatorial electrojet and the sq coupled systems? transfer entropy approach, *Adv. Space Res.*, *57*(9), 1859–1870.

Yahnin, A., and T. Yahnina (2007), Energetic proton precipitation related to ion–cyclotron waves, *J. Atmos. Sol. Terr. Phys.*, *69*(14), 1690–1706.

Yahnin, A., T. Yahnina, and H. Frey (2007), Subauroral proton spots visualize the Pc1 source, *J. Geophys. Res.*, *112*, A10223, doi:10.1029/2007JA012501.

Yahnina, T., A. Yahnin, J. Kangas, J. Manninen, D. Evans, A. Demekhov, V. Y. Trakhtengerts, M. Thomsen, G. Reeves, and B. Gvozdevsky (2003), Energetic particle counterparts for geomagnetic pulsations of Pc1 and IPDP types, *21*, 2281–2292.

Yuan, Z., Y. Xiong, Y. Pang, M. Zhou, X. Deng, J. G. Trotignon, E. Lucek, and J. Wang (2012), Wave-particle interaction in a plasmaspheric plume observed by a Cluster satellite, *J. Geophys. Res.*, *117*, A03205, doi:10.1029/2011JA017152.

Yumoto, K., and T. Saito (1980), Hydromagnetic waves driven by velocity shear instability in the magnetospheric boundary layer, *Planet. Space Sci.*, *28*(8), 789–798.